

ARTICLE

Received 28 May 2015 | Accepted 21 Sep 2015 | Published 23 Oct 2015

DOI: 10.1038/ncomms9696

OPEN

Defective titanium dioxide single crystals exposed by high-energy {001} facets for efficient oxygen reduction

Dan-Ni Pei^{1,*}, Li Gong^{1,*}, Ai-Yong Zhang^{1,2}, Xing Zhang¹, Jie-Jie Chen¹, Yang Mu¹ & Han-Qing Yu¹

The cathodic material plays an essential role in oxygen reduction reaction for energy conversion and storage systems. Titanium dioxide, as a semiconductor material, is usually not recognized as an efficient oxygen reduction electrocatalyst owing to its low conductivity and poor reactivity. Here we demonstrate that nano-structured titanium dioxide, self-doped by oxygen vacancies and selectively exposed with the high-energy {001} facets, exhibits a surprisingly competitive oxygen reduction activity, excellent durability and superior tolerance to methanol. Combining the electrochemical tests with density-functional calculations, we elucidate the defect-centred oxygen reduction reaction mechanism for the superiority of the reductive {001}-TiO_{2-x} nanocrystals. Our findings may provide an opportunity to develop a simple, efficient, cost-effective and promising catalyst for oxygen reduction reaction in energy conversion and storage technologies.

¹CAS Key Laboratory of Urban Pollutants Conversion, Department of Chemistry, University of Science and Technology of China, Hefei 230026, China.

²Department of Municipal Engineering, Hefei University of Technology, Hefei 230009, China. *These authors contributed equally to this work.

Correspondence and requests for materials should be addressed to A.Y.Z. (email: aiyzhang@ustc.edu.cn) or to H.Q.Y. (email: hqyu@ustc.edu.cn).

Increasing energy demands have stimulated intense research on alternative energy conversion and storage systems with a high efficiency, low cost and environmental benignity. The oxygen reduction reaction (ORR) has a key role in metal-air batteries and polymer membrane electrolyte fuel cells^{1,2}, but has become a bottleneck. ORRs traditionally require the exclusive use of platinum-based catalysts^{3,4}. Owing to the high cost of Pt and declining activity, alternative catalysts based on non-precious metal oxides, for example, Fe₃O₄, Co₃O₄ and so on, have been actively pursued^{5–11}. TiO₂ is a widely used semiconductor because of its Earth abundance, low cost, no toxicity and high stability¹². Thus, incorporating TiO₂ into energy conversion and storage systems is thus an attractive and promising idea. However, as a transition metal oxide, TiO₂ has not been considered as an efficient electrocatalyst because of its low conductivity and poor reactivity resulting from intrinsic insulating properties, for example, the wide bandgap energy ($E_g = 3.2$ eV) (ref. 12). Up to now, several works have been reported on the use of TiO₂ for ORR, but an overall low activity is obtained^{12–19}.

Tremendous efforts have been made to improve TiO₂ electrochemical properties. The non-stoichiometric reduction of TiO₂ is known to substantially narrow the bandgap to the semiconductor level (usually below 2.0 eV) and thus increases the donor density and electric conductivities as well as the overall catalytic performance, because of the incorporated structural defects, that is, oxygen vacancy and Ti³⁺ (refs 20–24). On the other hand, it is well documented that the ORR at MnO₂ proceeds through chemical oxidation of the surface Mn³⁺ generated by the discharge of MnO₂ with O₂ splitting, and thus the catalytic activity is dependent highly on the electrochemical redox activity of these species^{25–29}. Mn³⁺ is the active valence state for ORR, owing to its single e_g occupancy and thus the enhanced ability to stabilize ORR intermediates on the catalyst surface^{30–33}. For other Mn-based oxides, the high ORR activities are also proposed to be a result of surface non-stoichiometry and the presence of surface Mn³⁺ (ref. 29). In particular, Mn₃O₄ with a unique mixed-valence state has been used as an active catalyst, since the coexistence of Mn²⁺, Mn³⁺ and Mn⁴⁺ facilitates the formation of defects, that is, vacancies, electrons and holes, which govern the electronic distribution of Mn₃O₄ (refs 25–33).

The surface atomic structure, physiochemical properties and catalytic activity of TiO₂ are also highly shape- and facet-dependent³⁴. On the one hand, compared with randomly packed polycrystalline TiO₂, the well-defined single crystals (SCs) with a high crystalline usually possess a much higher electronic conductivity and lower electron transfer resistance because of their continuous and ordered interior crystal structure, which favours the separation and transfer of reactive photocarriers as well as the overall catalytic performance³⁴; on the other hand, compared with the thermodynamically stable {101} facet of TiO₂ crystals with a low surface free energy (0.44 J m⁻²), the arrangement and category of constituent atoms on the high-energy {001} facet (0.90 J m⁻²) govern its unique geometrical and electronic structures, and its surface functional groups considerably affect its stability, adsorptive property and catalytic activity³⁴. All these features make TiO₂ crystals with {001} facet highly efficient for various catalytic applications.

Inspired by these informative results and the crystal similarity between TiO₂ and MnO₂, we try to explore the feasibility of using the reduced non-stoichiometric TiO_{2-x} SCs containing the electro-conducting Ti³⁺ species and oxygen vacancies as an ORR catalyst in energy conversion and storage systems. Herein, we first prepare the defective facet-controlled TiO_{2-x} SCs self-doped by oxygen vacancy via a facile solvothermal process, followed by a high-temperature thermal treatment in the reductive H₂ atmosphere; then systematically explore the TiO_{2-x} SCs as a catalyst for ORR by both electrochemical tests and density-functional calculations (DFTs); at last, the reasons for the observed superiority of TiO_{2-x} SCs in ORR are investigated. The facet- and defect-engineered TiO_{2-x} SCs exhibit a surprisingly high ORR activity, excellent durability and superior tolerance to methanol, owing to their defect-centred oxygen reduction mechanism.

Results

Morphological and structural properties of TiO_{2-x} SCs. The morphology of the two prepared TiO₂ samples were highly truncated bipyramids of about 20 nm in diameter, with few one-dimensional nanorods randomly packed (Fig. 1a,b and Supplementary Fig. 1). The lattice fringe spacing of 0.35 nm corresponded to the {101} planes, whereas the lattice fringe spacing of 0.47 nm corresponded to the {002} planes for the defective {001}-TiO_{2-x} SCs (Fig. 1b), indicating that the top/bottom surface exposed by truncation was bound by a {001} facet. Moreover, the angle labelled in the corresponding fast-Fourier transform image inset was 68.3°, which is in good agreement with the theoretical value of the angle between the {101} and {001} planes. The clear lattice fringes for the non-defective {001}-TiO₂ SCs with an interplanar lattice spacing of 0.35 and 0.47 nm corresponded to the (101) and (002) atomic planes, respectively (Fig. 1d), and the angle labelled in the fast-Fourier transform image was also 68.3°. These results suggest that the morphology, structure and facet exposing of the defective {001}-TiO_{2-x} SCs were well retained after high-temperature calcination under oxygen-rich atmosphere (Fig. 1).

In the given F-free nonhydrolytic alcoholysis route, {001}-TiO_{2-x} SCs were formed via the controlled and smooth hydrolysis of TiCl₄ in absolute ethanol³⁵. Upon heating, ethanol was assumed to thermally react with dissolved oxygen and release water molecule (reaction 1), which coordinated to Ti⁴⁺ cations to form titanium oxy/hydroxychloride complex from polymerization/condensation. Then, TiO₂ was formed with these complexes as intermediates (reaction 2). In this process, Cl⁻ anions might act as the functional capping and shape controlling

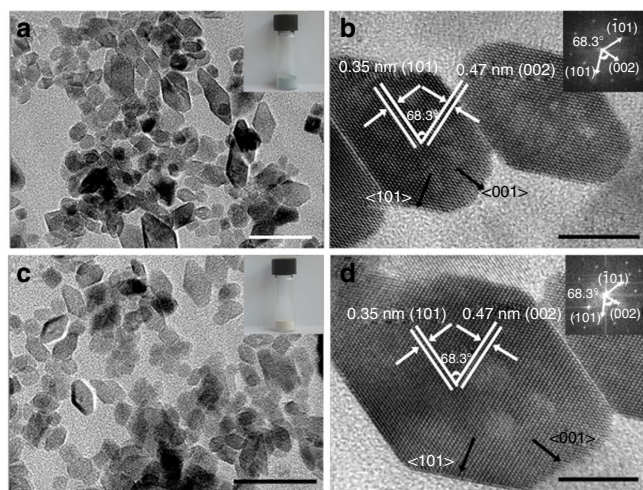
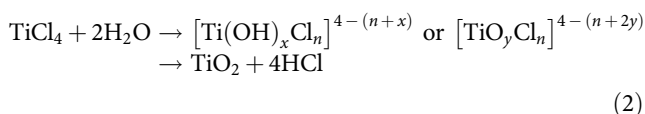


Figure 1 | Morphology and structure of different TiO₂ catalysts. Morphological (a,c) and structural (b,d) properties of the {001}-TiO_{2-x} SCs and {001}-TiO₂ SCs, the insets of b and d are their corresponding fast-Fourier transform patterns. Scale bars, 50 nm (a,c) and 10 nm (b,d).

reagent to favourably reduce the surface energy difference between the {001} and {101} facets³⁴.



Supplementary Figure 2a shows the X-ray diffraction (XRD) patterns of the TiO₂ polycrystals (PCs), TiO₂ SCs and TiO_{2-x} SCs, in which the diffraction peaks highly matched those of anatase TiO₂ (JCPDS No. 21-1272), whereas the broadening of the diffraction peaks of the two facet-engineered samples could be attributed to their relatively smaller crystal size³⁴. On the other hand, the reduced TiO_{2-x} sample displayed type IV nitrogen adsorption-desorption isotherms with hysteresis loops indicative of the mesoporous structure with narrow pore size distribution centred around 15.0 nm (Supplementary Fig. 2b). These mesopores were constructed by gathering nanoparticles into nanosheets, and the Brunauer–Emmett–Teller (BET) surface area was calculated as 47.0 m² g⁻¹ from the nitrogen adsorption-desorption isotherms.

Compared with the conventional F-mediated hydrothermal/solvothermal routes³⁴, the prepared TiO₂ SCs possessed a smaller particle size and thus a higher surface area. These might provide more reactive sites for their catalytic applications, whereas the exposed percentage of high-energy {001} was relatively lower. Furthermore, the TiO_{2-x} SCs prepared using the Zn-mediated alcoholthermal route in this work were very stable, and no obvious colour change was observed during its exposure in air even for over 1 year after their preparation. Their stability was comparable with the reduced TiO_{2-x} samples prepared by other methods^{20,21,23}. The metallic Zn not only served as a functional reductant for the reductive formation of Ti³⁺, but also further stabilized the newly generated oxygen vacancies and hence Ti³⁺ on the crystal surface and subsurface. It also increased the number of surface oxygen vacancies by weakening the surface-oxygen bonds and thus enhanced the overall catalytic activity of defective TiO_{2-x} polymorph³⁵.

ORR activity of TiO_{2-x} SC. Figure 2 shows that the ORR curves on both the rotating disk electrode (RDE) and the rotating ring-disk electrode (RRDE) were in the order of {001}-TiO_{2-x} SCs > {001}-TiO₂ SCs > {101}-TiO₂ PCs. The onset potential on the {101}-TiO₂ PCs was beyond -1.0 V, whereas it positively shifted to approximately -0.4 V on the {001}-TiO₂ SCs and further to -0.3 V on the {001}-TiO_{2-x} SCs (Fig. 2a), when the crystals were self-doped by oxygen vacancies and Ti³⁺ to form the reduced crystal structure. The cathodic current was also much higher on the facet- and defect-engineered TiO₂ sample (Supplementary Table 1). At the given potential of -0.40 V (versus saturated calomel electrode (SCE)), the measured current density increased from 1.88 μA cm⁻² on the {101}-TiO₂ PCs to 39.55 μA cm⁻² on the {001}-TiO₂ SCs and further to 180.06 μA cm⁻² on the {001}-TiO_{2-x} SCs (Fig. 2a).

The BET surface areas of the three involved TiO₂ samples exhibited no significant difference (47.0, 43.2 and 42.3 m² g⁻¹ for {001}-TiO_{2-x} SCs, {001}-TiO₂ SCs and {101}-TiO_{2-x} PCs, respectively; Supplementary Figs 2–4), and their gathering modes were identical, implying that these TiO₂ samples have comparable electrochemical activities. Thus, the observed significant ORR superiority of the {001}-TiO_{2-x} SCs over the {001}-TiO₂ and {101}-TiO₂ polymorphs should be attributed mainly to the surface defect and {001} exposure (Fig. 2), rather than other sources. Also, the identical chemical compositions, crystal

morphologies and structures of the {001}-TiO_{2-x} SCs and {001}-TiO₂ SCs (Fig. 1 and Supplementary Figs 2,4 and 5) rendered them comparable electrochemical ORR activities. This indicates that the observed ORR activity difference between the two TiO₂ samples dominantly originated from the defective crystal defects, oxygen vacancies and reduced Ti³⁺, rather than other sources. Moreover, the presence of coordination-unsaturated titanium sites increased the carrier density and facilitated the molecular diffusion of oxygen along the conducting crystal channels of the non-stoichiometric TiO_{2-x} SCs. The added Zn, served as both a reductant and a stabilizer, existed mainly in the form of ZnO clusters and dispersed on the TiO₂ surface owing to the larger ionic radii of Zn²⁺ (0.88 Å) than Ti⁴⁺ (0.745 Å) (ref. 35). However, the incorporation of such a small amount of foreign ZnO as impurity, that is, ~0.80 atom % in this work (Supplementary Fig. 5), would not bring about any ORR interference because of its low electrochemical activity as a wide bandgap n-type semiconductor^{36,37}.

The number of transferred electrons in ORR, *n*, was calculated from the slopes of straight lines at different potentials using the Koutecky–Levich model (Supplementary Figs 6 and 7), and a continuous increase in *n* with the increasing overpotential was observed. Specifically, the calculated electron transfer number, *n*, was 0.44 at -0.4 V versus SCE and 2.41 at -1.3 V versus SCE for the defective {001}-TiO_{2-x} SCs (Fig. 2c), whereas only 0.26–2.34 and 0.00–0.59 for the perfect {001}-TiO₂ SCs and the commercial {101}-TiO₂ PCs, respectively. These calculation results indicate that the cathodic ORR on the three TiO₂ polymorphs under the given conditions, from -0.4 V to -1.3 V versus SCE, was dominantly via the two-electron pathway with a high overpotential.

Such a two-electron pathway was further validated by the RRDE results (Fig. 2d) and is highly consistent with the DFT calculations. In the RRDE tests, the electrode modified with the defective {001}-TiO_{2-x} SCs generated a notable ring current, *I_r*, over the whole potential range from the onset potential in 0.1 M KOH aqueous solution. This indicates the favourable and dominant generation of HO₂⁻ intermediate in the electrochemical reduction. Specifically, for the defective {001}-TiO_{2-x} SCs, the measured H₂O₂ yield (HO₂⁻ % in alkaline solution) was 111.06% at the potential of -0.4 V versus SCE, and became 94.20% at -1.3 V versus SCE (Supplementary Fig. 8). The calculated electron transfer number, *n*, from the RRDE tests varied in a range of 1.78–2.17 with the potential of -0.4 to -1.3 V versus SCE (Supplementary Fig. 8). These RRDE results are consistent with the RDE results, suggesting that the ORR on the defective {001}-TiO_{2-x} SCs proceeded mainly via a two-electron pathway.

Considering the low electric conductivity and poor dispersity of nano-sized metal oxide catalysts, some nano-structured carbonaceous supports are usually needed in ORR tests¹⁸. Herein, all the TiO₂ samples were mixed with the commercial Cabot carbon nanoparticles (Vulcan XC-72R, USA) as a conductive support. The same trend of ORR activity, {001}-TiO_{2-x} SCs/C > {001}-TiO₂ SCs/C > {101}-TiO₂ PCs/C, was also observed (Supplementary Table 1). The {001}-TiO_{2-x} SCs was hydrothermally deposited on reduced graphene oxide (rGO) to form the {001}-TiO_{2-x} SCs/rGO hybrid, and it exhibited a further enhanced capacity for ORR (Fig. 2e,f). Interactions between rGO and metal oxide indicate a possible charge transfer across the interface depending on the hybrid interface spacing and the Fermi level difference, which might be the main reason for the enhanced ORR activity^{10,11}. In addition, all linear sweep voltammetry (LSV) curves exhibited a slow current increase and no current plateau (Supplementary Figs 6 and 9), indicating the two-electron reduction of O₂ to OOH⁻. All these

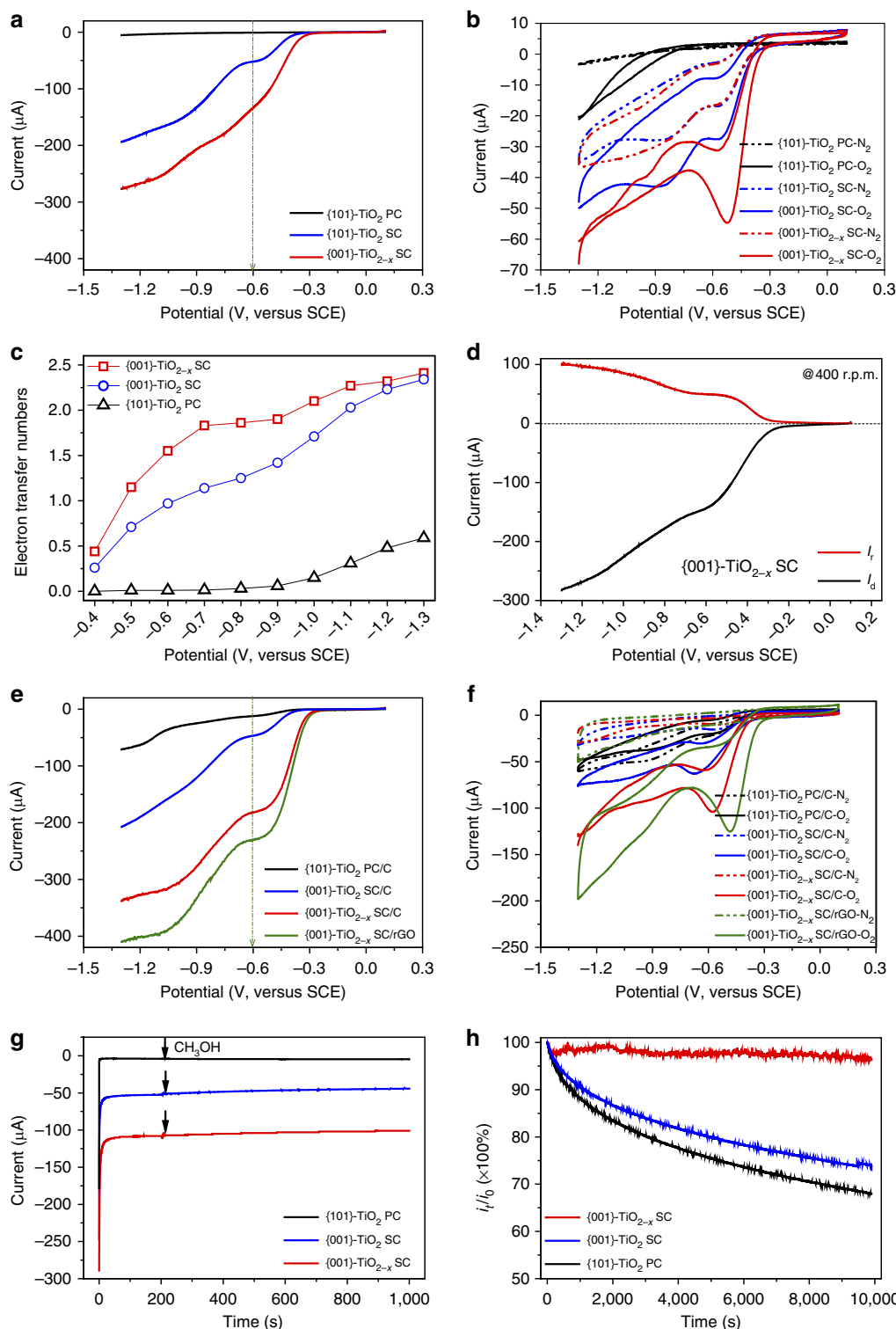


Figure 2 | ORR properties on different TiO_2 catalysts. Linear sweep voltammetry in O_2 -saturated 0.1M aqueous KOH electrolyte solution at a scan rate of 10 mV s^{-1} at 400 r.p.m. (**a,e**) and cyclic voltammetry in N_2 - and O_2 -saturated 0.1M KOH at a scan rate of 10 mV s^{-1} at 400 r.p.m. (**b,f**) electron transfer numbers calculated from the K-L model as a function of electrode potential (**c**) RRDE test on the defective TiO_{2-x} in O_2 -saturated 0.1M aqueous KOH electrolyte solution at a scan rate of 10 mV s^{-1} at 400 r.p.m. (**d**) chronoamperometric responses obtained at -0.45 V in O_2 -saturated 0.1M KOH at 200 r.p.m. with the addition of 10 vol.% methanol (**g**) and cathodic current stability obtained at -0.45 V in O_2 -saturated 0.1M KOH at 200 r.p.m. (**h**).

results clearly indicate that both the exposed high-index {001} facet and the engineered oxygen vacancy contributed to the enhanced ORR activity of the TiO_2 catalyst.

The long-time ORR stability was evaluated using chronoamperometric response at -0.45 V in O_2 -saturated 0.1M KOH

aqueous solution (Fig. 2g,h). The defective TiO_{2-x} SCs exhibited excellent stability, retaining more than 95% of the initial current even after 10,000 s, whereas both the TiO_2 SCs and TiO_2 PCs lost nearly 30% of the initial current. Moreover, all TiO_2 samples showed superior selectivity to ORR with no obvious current

change after adding methanol. In addition, the TiO_{2-x} SCs also survived in the highly corrosive electrolyte (6 M KOH aqueous solution), demonstrating its high activity, favourable kinetics and excellent stability. The observed superior ORR stability of the defective TiO_{2-x} SCs should be attributed mainly to the excellent stability of the surface-engineered Ti^{3+} species, because the metallic Zn not only served as a chemical reductant for the reductive formation of Ti^{3+} but also further stabilized the newly generated oxygen vacancies and Ti^{3+} on the crystal surface and subsurface³⁵. The poor ORR catalytic stability of the TiO_2 PCs was probably owing to their anatase-rutile mixed crystal phase^{38,39}.

The above results clearly show that the ORR activity of TiO_2 was substantially enhanced by a simple facet- and defect-engineering strategy. It is noted that the prepared defect-engineered TiO_{2-x} with exposed high-energy {001} facets still exhibited a lower ORR activity than Fe_3O_4 and Mn_3O_4 (refs 10,32), the two most typical metal oxide ORR electrocatalysts, with a more negative onset potential of ca. -0.30 V and a lower cathodic current density of ca. 1.0 mA cm⁻² (Fig. 2a,b). On the other hand, its ORR stability was much higher than the commercial Pt/C benchmark, as the chronoamperometric response remained intrinsically unchanged on the TiO_{2-x} while more than 20% decrease was observed on the Pt/C benchmark during the given 10,000 s (refs 4,5,9). Moreover, TiO_2 is intrinsically characterized of Earth abundance, low cost, high stability and environmental compatibility for industrial applications.

Ti^{3+} and its roles on TiO_{2-x} SCs. The surface Ti oxidation state was probed by Fourier transform infrared (FTIR) spectroscopy, diffuse reflectance spectra, X-ray photoelectron spectroscopy (XPS), electron spin resonance (ESR) and Raman spectra, respectively (Fig. 3). The FTIR spectrum exhibited two distinct -OH stretching bands at 3,400 and 1,632 cm⁻¹ (Fig. 3a), indicating the presence of oxygen vacancies and/or reductive Ti^{3+} as the reactive adsorption sites for water molecules and hydroxyl ions. The wider -OH absorption bands also suggest that the -OH groups experienced a more varied environment on the defective {001}- TiO_{2-x} SCs. In high-resolution XPS, an obvious shoulder appeared in the low-energy range (457.5–455.5 eV) of the Ti 2p spectrum, which might be attributed to Ti^{3+} in the TiO_2 lattice (Fig. 3c,d)²². This was further confirmed by the ESR spectrum with the strong signals around $g=1.95$ and $g=2.00$, respectively²², but no significant signal indicative of surface Ti^{3+} was observed at $g=2.02$ because of the surface oxidation (Fig. 3e). Moreover, the measured Raman spectra also confirmed the presence of more oxygen vacancies in the reduced TiO_2 SCs, owing to the positive peak shift, which was resulted from the modified geometric and surface structures (Fig. 3f)²³.

In principle, the Ti^{3+} species were generated from the reduction of Ti^{4+} under reductive conditions and the *in situ* Ti^{3+} -doped TiO_2 displayed oxygen vacancies because of the replacement of Ti^{4+} by Ti^{3+} in the lattice^{20–24}. Meanwhile, the {001} facet contained more oxygen vacancies than the {101} facet, because each Ti in the {001} facet coordinated with 5 oxygen atoms, whereas each Ti in the {101} facet coordinated with either 5 or 6 oxygen atoms in the probability around 50% to 50% (ref. 34). The presence of Ti^{3+} and the oxygen vacancies resulted in some new energy levels below the conduction band of the TiO_2 (refs 22,23), leading to an obvious spectral response in visible range (Fig. 3b). Such a photon excitation in the infrared region indicates that the formed Ti^{3+} was dominantly derived from oxygen deficiency²⁴. In addition, the oxygen-deficient TiO_2 SCs

had different Raman spectra from the oxygen-free analogue, but they shared nearly the same XRD patterns. This result indicates that most oxygen deficiency-related Ti^{3+} should mainly locate on the surface and subsurface of the crystals²¹.

The presence of these structural defects played important roles in the electro-catalytic properties of the TiO_{2-x} . The enhanced visible light adsorption on the reduced TiO_2 SCs (Fig. 3b) indicates that the introduced new energy states by Ti^{3+} self-doping mainly laid below the bottom of conduction band, and these electro-conducting Ti^{3+} could significantly narrow the inherent bandgap and enhance the electrical conductivity (Fig. 4a and Supplementary Fig. 10). In addition, both TiO_2 samples exhibited positive slopes as expected for n-type semiconductors, and a higher electron density was obtained for the TiO_{2-x} SCs from the slope of Mott–Schottky plot (Fig. 4b)²¹. Thus, although the TiO_{2-x} SCs were not the direct bandgap semiconductor (Fig. 3b), significant modifications of their electric structures occurred during the self-doping process, which contributes to their higher electron density. Moreover, all these enhanced electrochemical conductivity, reduced electron transfer resistance and improved interfacial capacity on the TiO_{2-x} SCs derived from the second semicircles in electrochemical impedance spectroscopy (associated with the fast reaction kinetics and considerable increases in the electrochemically accessible surface) are essential for an efficient ORR catalyst.

Lowering the electrochemical overpotentials for both hydrogen evolution reaction (HER) and oxygen evolution reaction (OER) favours their efficient applications. In this work, both much reduced overpotentials and substantially enhanced currents were obtained on the defective {001}- TiO_{2-x} SCs for both HER and OER (Fig. 4c,d). For example, the cathodic current at the selected -0.3 V (versus SCE) and the anodic current at the selected $+1.2$ V (versus SCE) were -1.9 μA and 12.3 μA on the {101}- TiO_2 PCs, -7.5 μA and 20.2 μA on the {001}- TiO_2 SCs and -25.7 μA and 185.6 μA on the {001}- TiO_{2-x} SCs, respectively. The catalytic activity order of {001}- TiO_{2-x} SCs > {001}- TiO_2 SCs > {101}- TiO_2 PCs indicates that the introduction of defective oxygen vacancies uniformly into TiO_2 lattice and the exposed high-energy {001} facets could substantially improve their catalytic performance.

Catalytic mechanism of TiO_{2-x} for ORR. The ORR is affected by the chemical composition, elemental valence, crystal structure and surface state^{5–11}. Also, the adsorption configuration of surface oxygen molecule and the corresponding strength of oxygen binding also impact with the ORR activities. In this work, the enhanced ORR activity on the defective {001}- TiO_{2-x} SCs might be highly associated with the single-crystalline structure, the exposed high-energy {001} facet and the Ti multiple valences caused by the defective oxygen vacancies (Fig. 5). First, the significant enhancement of electric conductivity from both the continuous and ordered interior structure and the enhanced crystallinity should greatly favour fast electron transfer (that is, higher charge mobility) and reduce electrode polarization in ORR. Second, the exposed high-energy {001} facet with unique atomic, electronic and energetic structure could ensure its significant ORR activity because of its facet-mediated behaviours in dissociative adsorption and charge mobility³⁴. Last, the active valence state of defective Ti^{3+} originating from engineered oxygen vacancies could play a governing role in ORR and thus the enhanced ability to stabilize intermediates on catalyst surface owing to its single e_g occupancy⁴⁰.

In TiO_2 , the missed oxygen atom from the bulk or surface is taken by one or two ‘free’ electrons in the defective crystal, and the three nearest Ti atoms tend to relax away from the vacancy in

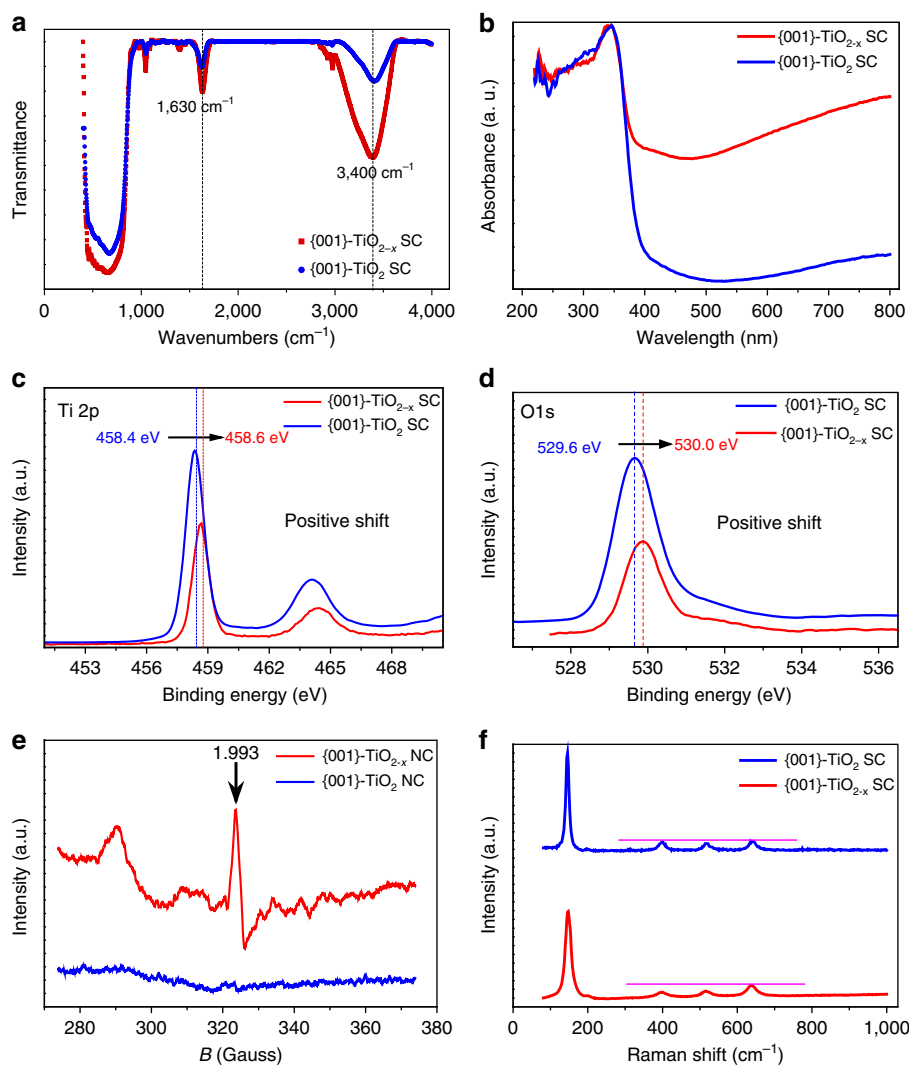
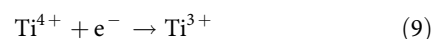
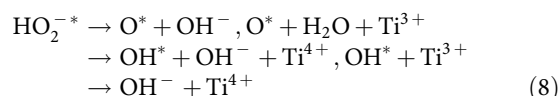
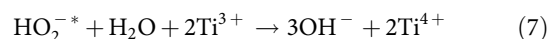
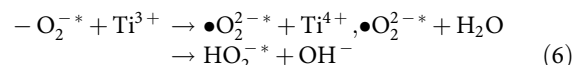
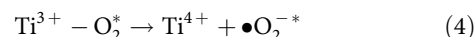
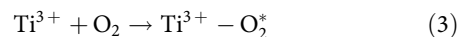


Figure 3 | Defects in TiO_{2-x} SCs. Determination of defective Ti^{3+} in the {001}-engineered TiO_{2-x} SCs: FTIR (a), diffuse reflectance spectra (b), XPS (c,d), ESR (e) and Raman (f).

order to strengthen their bonding with the rest of the lattice²⁰. Thus, the defect-related properties mainly include structural, electronic, optical, dissociative adsorption and reductive properties²¹. For ORR, the chemical adsorption and dissociative activation of O_2 on the TiO_2 surface is a governing step, yet it has been well documented that both of the two processes are thermodynamically favoured only on the defective negative site, rather than the perfect neutral site^{22,23}. In principle, the dissociated adsorption of O_2 on the defective oxygen vacancy could result in more efficient electron-transfer process and greater ORR kinetics because of the strong coupling between the adsorbate and the surface, and are intimately related to the overall catalytic performance.

On the defective {001}- TiO_{2-x} SC, O_2 is first selectively adsorbed onto the defective subsurface oxygen vacancy with a much higher adsorption energy (reaction 3), as it only adsorbs onto the site where excess negative charge is available to form O-Ti bond; then, the chemically adsorbed O_2 could capture the free electrons located on oxygen vacancy site, simultaneously producing superoxide radical groups (reaction 4). The formation of these radical groups is effective to promote charge separation as well as the reduction of O_2 via either a two-electron pathway (reactions 5 and 6) or a 4-electron pathway (reactions 7 and 8), followed by the reduction of Ti^{4+} to Ti^{3+} (reaction 9). In this

defect-centred ORR (Fig. 5), the possible catalytic disproportionation of hydrogen peroxide occurs (reactions 7 and 8), which might be the overall rate-limiting step of the ORR.



The DFT calculations further indicate that the four- and fivefold coordinated vacancy-surrounding titanium sites assume their respective role in oxygen adsorption and reactive activation, which lower the activation barrier and avoid catalytic poisoning.

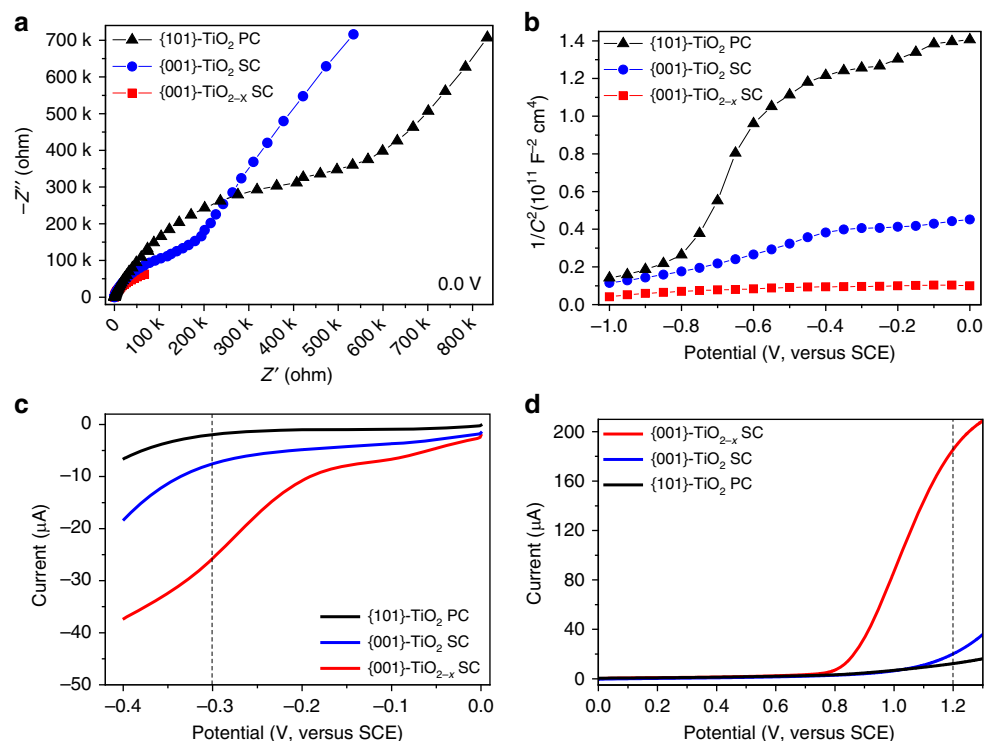


Figure 4 | Ti^{3+} -induced properties of TiO_{2-x} SCs. Role of defective Ti^{3+} in the electronic and electrochemical properties of the {001}-engineered TiO_{2-x} SCs: electrochemical impedance spectroscopy (a), Mott-Schottky (b), HER (c) and OER (d).

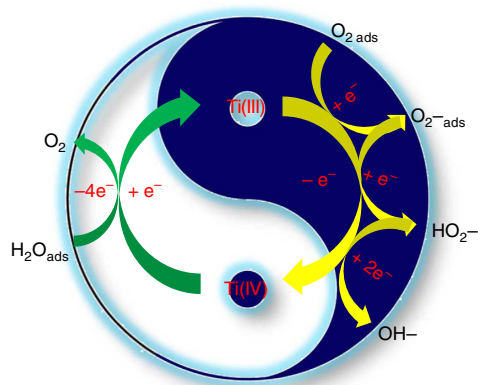


Figure 5 | Defect-centred ORR mechanism on TiO_{2-x} SCs. The mixed-valence Ti species cycling between +3 and +4 states at oxygen vacancy sites in the defective TiO_{2-x} SCs thermodynamically served as the reactive sites for cathodic oxygen reduction.

On the one hand, oxygen was found to be strongly bound onto the {001}- TiO_{2-x} with the highest adsorption energy of 2.28 eV (Table 1 and Supplementary Note 1); on the other hand, based on the optimized geometry structures of adsorption configuration (Fig. 6), the free energies (G) of key intermediates, O_2^{2-*} , O_2^{2-*} , HOO^{-*} , OH^* and O^* (*: adsorbed state; Supplementary Table 2 and Supplementary Note 1), and free energy changes (ΔG) of each step of ORR, in Fig. 7a, were further calculated (Supplementary Table 3) and the favourable energy profile is plotted on {001}- TiO_{2-x} (Fig. 7b). First, the ΔG of -3.297 eV for O_2^{2-*} formation is the lowest on {001}- TiO_{2-x} , compared with that of 3.945 and -2.478 eV on {101}- TiO_2 and {001}- TiO_2 ; second, for the overall rate-limiting ORR step of regenerating hydroxide from adsorbed oxide, {001}- TiO_{2-x} affords the lowest energy barrier of only 5.01 eV, compared with that of 10.58 and

Table 1 | Adsorption energy (ΔE_{ads}) for the three different adsorption configurations of O_2 on {001}- TiO_2 and {001}- TiO_{2-x}

System	E_{surf} (eV)	E_{react} (eV)	E_{system} (eV)	ΔE_{ads} (eV)
{001}- TiO_{2-x}	-20,794.63	-857.85	-21,654.76	2.28
{001}- TiO_2	-21,226.38	-857.85	-22,085.26	1.03

7.55 eV on {101}- TiO_2 and {001}- TiO_2 ; at last, the total ΔG from adsorbed O_2 to 4OH^- on {001}- TiO_2 , {001}- TiO_{2-x} and {101}- TiO_2 is -3.608 , -7.741 and -2.806 eV, respectively. All these results not only confirm that {001}- TiO_2 was thermodynamically and kinetically more active than {101}- TiO_2 , but also show that oxygen vacancies on {001}- TiO_{2-x} effectively increased its catalytic activities. This conclusion is consistent with the electrochemical results (Fig. 2 and Supplementary Figs 6 and 9).

Although the further reduction of the generated peroxide on the defective {001}- TiO_{2-x} SCs showed a high-energy barrier of 5.01 eV, its Gibb's free energy was -4.43 eV (Supplementary Table 3), indicating that this step could spontaneously occur at room temperatures despite of a low reaction rate. Thus, the ORR reaction equilibrium was able to gradually shift to the reaction direction of deep oxygen reduction. Moreover, this theoretical ORR rate-controlling step with such a high-energy barrier for the subsequent reduction of the as-generated peroxide from the DFT calculations was further validated by both the RDE and RRDE tests. The calculated electron transfer number and peroxide percentage were $\sim 2.2\%$ and $\sim 95\%$, respectively, even at a highly negative -1.3 V versus SCE on the defective {001}- TiO_{2-x} SCs (Fig. 2c and Supplementary Fig. 8). Also, the geometric structural changes of this rate-controlling step were simple and lie in the last H_2O dissociation and OH^* generation. Thus, the series two-electron mechanism is the sole ORR pathway for this step.

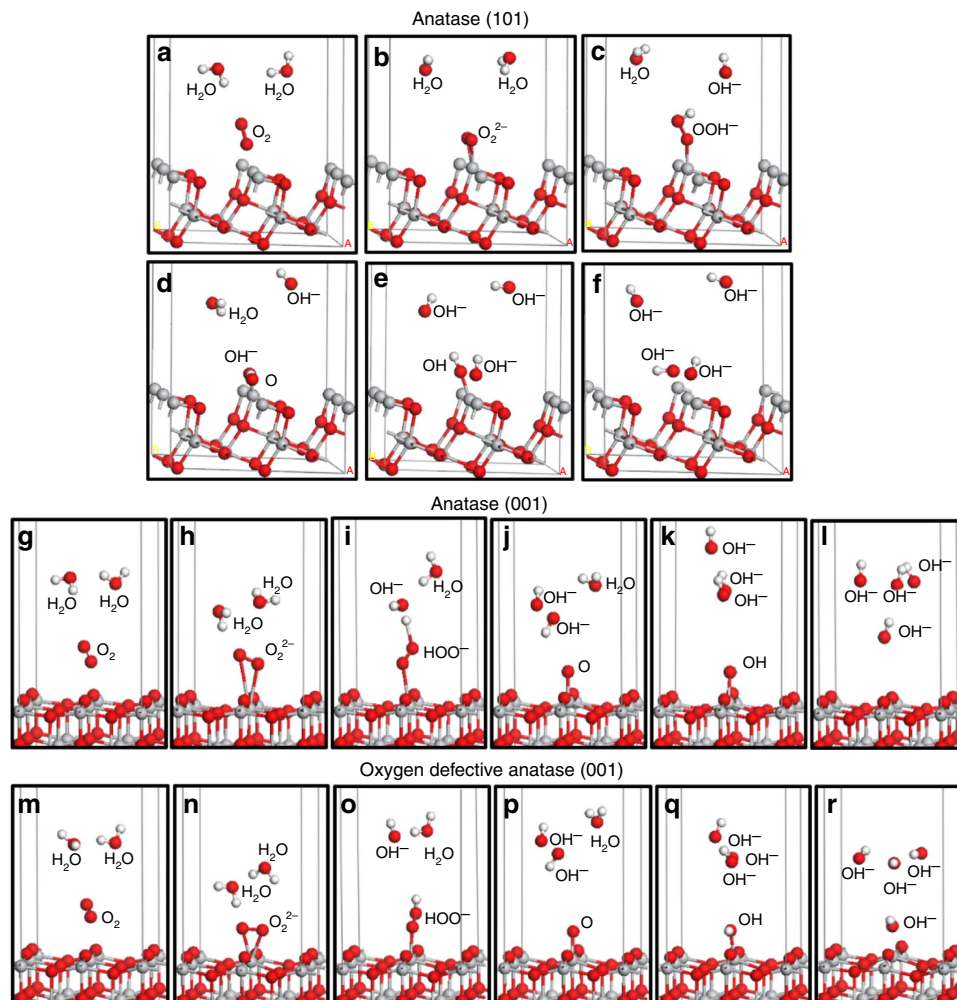


Figure 6 | Geometry structures of adsorption configuration. Optimized structures of each step in ORR on the {101}-TiO₂, {001}-TiO₂ and {001}-TiO_{2-x}. (**a,g,m**) Initial structure, (**b,h,n**) O₂²⁻*, (**c,i,o**) HOO⁻*, (**d,j,p**) O*, (**e,k,q**) OH* and (**f,l,r**) OH⁻, white, red and grey spheres indicate H, O and Ti atoms, respectively.

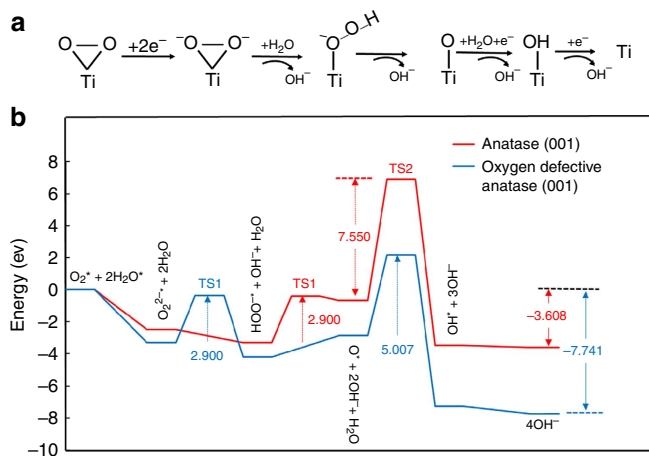


Figure 7 | ORR mechanism and energy profiles. DFT-calculated ORR mechanism on the anatase TiO₂ surface (**a**), and the energy profiles of ORR on the {001}-TiO₂ and {001}-TiO_{2-x}, TS represents transition states (**b**).

Discussion

This mixed-valence in the defective TiO_{2-x} as the most active catalyst for defect-centred ORR is also consistent with the previous design principle for perovskite catalysts, especially on Mn-based oxides^{25–33}. In addition, as the ORR involves the

oxidation and reduction of surface-defective Ti species, the number and activity of these redox centres could be important factors to define the overall catalytic performance.

In summary, we show that the new form of TiO₂ polymorph with defective crystal structure can be exploited as a promising ORR catalyst with a competitive activity, excellent durability and sufficient selectivity. The exposed high-energy {001} facets of the TiO₂ SCs is advantageous for oxygen interfacial adsorption and dissociative activation in ORR process. Moreover, the crystal oxygen vacancies and reductive Ti³⁺ sites further guarantee a durable and facile ORR process via a defect-centred mechanism. Our findings might open up a new avenue for efficient energy conversion and storage technologies based on the Earth-abundant, scalable, non-precious metal catalysts.

Methods

TiO_{2-x} SCs preparation. The reduced TiO_{2-x} SCs engineered by the high-index {001} facet were prepared using a modified solvothermal method³⁴. Briefly, at room temperature (10–15 °C), 2-ml TiCl₄ solution was slowly added into the absolute ethanol (40 ml) under vigorous stirring to form a transparent solution; then a given amount of metallic zinc powders with Ti/Zn molar ratio of 4:1 was added into the solution and magnetically stirred for over 1 h, in which process the solution colour gradually became blue; the obtained solution was immediately transferred into a 50-ml Teflon-lined stainless steel autoclave and was kept under 200 °C for 24 h; after this solvothermal treatment and being cooled down to room temperature, the solution was subjected to high-speed centrifugation; the precipitate was collected and repeatedly washed with EtOH and water for several times, dried in vacuum at 60 °C and finally ground to obtain blue-coloured Ti³⁺ self-doped

TiO_{2-x} for use. For comparison, the commercial TiO₂ PCs with low-index {101} facet (P25, Degussa Co., mean particle size of about 25 nm, anatase/rutile = 80:20, BET surface area of 50 m² g⁻¹) and the oxidized TiO_{2-x} SCs calcinated at 600 °C for 2 h under oxygen-rich atmosphere were used for reference.

Material characterization. The morphology and structure were characterized by high-resolution transmission electron microscopy (JEM-2100, JEOL Co.). XRD (X'Pert, PANalytical BV) was used to analyse the crystal structure. The diffuse reflectance spectra were measured on a ultraviolet-visible spectrophotometer (UV 2550, Shimadzu Co.). The chemical compositions were characterized using XPS (PHI 5600, Perkin-Elmer Inc.) and Raman spectrum (LABRAM-HR, JY Co.). The electronic state of Ti and O atoms were measured to provide structural information by ESR (JES-FA200, JEOL Co.). The surface area was measured using the BET method with a Builder 4200 instrument (Tristar II 3020M, Micromeritics Co.) at liquid nitrogen temperature. The infrared spectra were recorded between 4,000 and 400 cm⁻¹ with a FTIR spectrometer (Magna-IR 750, Nicolet Instrument Co.) using a potassium bromide disc technique.

Electrochemical characterization. All electrochemical measurements were carried out in a home-made three-electrode system, with pure and modified TiO₂ SCs deposited on glass carbon as the working electrode, Pt wire as the counter electrode and Ag/AgCl (KCl, 3 M) as the reference electrode. Electrochemical impedance spectroscopy analysis was conducted by applying an AC voltage amplitude of 5 mV within the frequency range from 10⁵ to 10⁻² Hz in 10 g l⁻¹ NaCl aqueous solution; Mott-Schottky plots were measured in 0.1 M Na₂SO₄ aqueous solution by impedance measurement at the fixed frequency of 1,000 Hz between the applied voltage range of 0–1 V; HER and OER were carried out in 0.5 M H₂SO₄ aqueous solution and 0.1 M KOH aqueous solution, respectively, at a scan rate of 50 mV s⁻¹.

ORR tests. Electrochemical ORR, LSV and cyclic voltammetry measurements, on the glass carbon RDE (dimension of 5 mm, geometric surface area of 0.196 cm²; Pine Research Instrumentation Inc.), were performed using a computer-controlled potentiostat (CHI 760D, CH Instrument) with a three-electrode glass electrochemical cell. The TiO₂ sample (2.0 mg) was dispersed in 2 ml absolute iso-propanol solvent. After applying ultrasonification for 30 min, 20 μl of the homogeneous suspension was dropped and the TiO₂ nanoparticles were adhered to the RDE using Nafion solution (5 μl, 0.05 wt. %) with a catalyst loading of ~0.10 mg cm⁻². The ink was dried slowly in open air and the drying condition was adjusted by trial and error until a uniform catalyst distribution across the electrode surface was obtained^{5,9}. The RDE loaded with different TiO₂ samples was used as the working electrode, an SCE as the reference electrode, and a Pt wire, as the counter electrode. The electrochemical ORR tests were conducted in either N₂- or O₂-saturated electrolyte (with 0.1 M KOH) at room temperature (10–15 °C). After purging O₂ or N₂ in the electrolyte for 30 min, the potential range was cathodically scanned between -1.3 and +0.1 V versus SCE at a scan rate of 10 mV s⁻¹. The LSV measurements were conducted at different rotating speeds from 400 to 1,600 r.p.m., using a Pine Model, whereas the cyclic voltammetry measurements were carried out without electrode rotating. In the ORR tests, the working electrode was cycled at least 15 times before electrochemical data were recorded, and a continuous flow of N₂ or O₂ was maintained to ensure saturation in supporting electrolyte. The ORR kinetic parameters are calculated using the Koutecky–Levich model:

$$\frac{1}{i} = \frac{1}{i_k} + \frac{1}{B \times \omega^{1/2}} \quad (10)$$

where i is the measured current, i_k is the kinetic current and ω is the electrode rotation rate.

The theoretical value of the Levich slope (B) is evaluated from the following equation:

$$B = 0.62 \times n \times F \times C_{O_2} \times D_{O_2}^{1/2} \times \nu^{1/2} \quad (11)$$

where n is the electron transfer number in ORR, F is the Faradic constant (96,485 C mol⁻¹), C_{O_2} is the saturated oxygen concentration in 0.1 M KOH aqueous solution (1.2 × 10⁻⁶ mol cm⁻³), D_{O_2} is the oxygen diffusion coefficient (1.73 × 10⁻⁵ cm² s⁻¹) and ν is the kinematic viscosity of the solution (0.01 cm² s⁻¹).

Electrochemical ORR measurements on the glass carbon RRDE (disk electrode: dimension of 5 mm, geometric surface area of 0.196 cm²; Pine Research Instrumentation Inc.) were carried out by the same procedures as on the RDE. The disk electrode was scanned cathodically at a rate of 10 mV s⁻¹ and the ring potential was kept constant at +0.3 V versus SCE. The HO₂⁻ percentage and the electron transfer number, n , are determined by the following equations:

$$\%(\text{HO}_2^-) = 200 \times \frac{I_r/N}{I_d + I_r/N} \quad (12)$$

$$n = 4 \times \frac{I_d}{I_d + I_r/N} \quad (13)$$

where I_d is disk current, I_r is ring current and N is current collection efficiency of the Pt ring, which was determined to be 0.40 from the reduction of K₃Fe(CN)₆.

DFT calculations. DFT calculations were carried out using the ultrasoft pseudopotential for electronic-ion interactions and generalized gradient approximation with the Predev–Burke–Ernzerhof exchange for exchange-correlation functional in the supercell approach as implemented in CASTEP program^{41,42}. The convergence criteria was set out to be *express*, and the tolerances of the energy was 1 × 10⁻³ eV per cell. The norm-conserving pseudopotential was constructed using the pseudopotential generator implemented in CASTEP. The energy cutoff of 750 eV for the plane wave basis was used throughout the study. The Brillouin zone integration was obtained with variable numbers of k -points, depending on the unit cell size and shape, generated by the Monkhorst-pack algorithm. Phonon dispersion and density of states were computed using the method of Finite displacement. The linear synchronous transit/quadratic synchronous transit methods were employed to search for the transition state structure and acquire the activation energy (E_a) of ORR⁴³.

The adsorption energy (ΔE_{ads}) was calculated to estimate the strength of a molecule–surface interaction and to seize the most energetically stable adsorption model. The ΔE_{ads} could be expressed as:

$$\Delta E_{\text{ads}} = E_{\text{surf}} + E_{\text{react}} - E_{\text{system}} \quad (14)$$

where the total energy values E_{system} , E_{surf} , E_{react} are relative to supercells simulating a molecule interacting with anatase TiO₂ surfaces, the surfaces and an isolated molecule in the vacuum, respectively.

The Gibb's free energy difference (ΔG) of each elementary reaction was given by the following equation:

$$\Delta G = \Delta E + \Delta ZPVE - T\Delta S \quad (15)$$

where ΔE is the total energy change, directly obtained from DFT calculations, $\Delta ZPVE$ is the change in zero-point energies, T is temperature (298.15 K) and ΔS is the change in entropy.

For the surface models, a vacuum region of 15 Å was embedded along surface to avoid the unwanted interaction between the slab and its period images. The {001}-TiO₂ surface had fivefold coordinated Ti atoms only, interconnected at the surface by two-coordinate bridging oxygen atoms, whereas the {101}-TiO₂ surface exhibited a sawtooth-like corrugation consisting of 5-coordinate and 6-coordinate Ti atoms as well as 2-coordinate and 3-coordinate oxygen atoms. In addition, according to the experiments, the {001}-TiO_{2-x} surface was constructed from the perfect {001}-TiO₂ surface model with a subsurface oxygen vacancy.

References

- Adler, S. B. Factors governing oxygen reduction in solid oxide fuel cell cathodes. *Chem. Rev.* **104**, 4791–4844 (2004).
- Zhang, J. T., Zhao, Z. H., Xia, Z. H. & Dai, L. M. A metal-free bifunctional electrocatalyst for oxygen reduction and oxygen evolution reactions. *Nat. Nanotechnol.* **10**, 444–452 (2015).
- Cheng, F. Y., Shen, J., Peng, B., Pan, Y. D., Tao, Z. L. & Chen, J. Rapid room-temperature synthesis of nanocrystalline spinels as oxygen reduction and evolution electrocatalysts. *Nat. Chem.* **3**, 79–85 (2011).
- Li, Y. G. *et al.* An oxygen reduction electrocatalyst based on carbon nanotube-graphene complexes. *Nat. Nanotechnol.* **7**, 394–400 (2012).
- Liang, Y. *et al.* Co₃O₄ nanocrystals on graphene as a synergistic catalyst for oxygen reduction reaction. *Nat. Mater.* **10**, 780–786 (2011).
- Suntivich, J. *et al.* Design principles for oxygen-reduction activity on perovskite oxide catalysts for fuel cells and metal-air batteries. *Nat. Chem.* **3**, 546–550 (2011).
- Cheng, F. Y. *et al.* Enhancing electrocatalytic oxygen reduction on MnO₂ with vacancies. *Angew. Chem. Int. Ed.* **52**, 2474–2477 (2013).
- Cheng, F. Y. & Chen, J. Transition metal vanadium oxides and vanadate materials for lithium batteries. *J. Mater. Chem.* **21**, 9841–9848 (2011).
- Liang, Y. Y. *et al.* Oxygen reduction electrocatalyst based on strongly coupled cobalt oxide nanocrystals and carbon nanotubes. *J. Am. Chem. Soc.* **134**, 15849–15857 (2012).
- Wu, Z. S. *et al.* 3D nitrogen-doped graphene aerogel-supported Fe₃O₄ nanoparticles as efficient electrocatalysts for the oxygen reduction reaction. *J. Am. Chem. Soc.* **134**, 9082–9085 (2012).
- Guo, S. J., Zhang, S., Wu, L. H. & Sun, S. H. Co/CoO nanoparticles assembled on graphene for electrochemical reduction of oxygen. *Angew. Chem. Int. Ed.* **51**, 11770–11773 (2012).
- Liu, B. *et al.* Large-scale synthesis of transition-metal-doped TiO₂ nanowires with controllable overpotential. *J. Am. Chem. Soc.* **135**, 9995–9998 (2013).
- Choi, Y. K., Seo, S. S., Chjo, K. H., Choi, Q. W. & Park, S. M. Thin titanium dioxide film electrodes prepared by thermal oxidation. *J. Electrochem. Soc.* **139**, 1803–1807 (1992).
- Kim, J. H., Ishihara, A., Mitsushima, S., Kamiya, N. & Ota, K. I. Catalytic activity of titanium oxide for oxygen reduction reaction as a non-platinum catalyst for PEFC. *Electrochim. Acta* **52**, 2492–2497 (2007).

15. Boskovic, I., Mentus, S. V. & Pjescic, M. Electrochemical behavior of an Ag/TiO₂ composite surfaces. *Electrochim. Acta* **51**, 2793–2799 (2006).
16. Berger, T., Monllor-Satoca, D., Jankulovska, M., Lana-Villarreal, T. & Gmez, R. The electrochemistry of nanostructured titanium dioxide electrodes. *ChemPhysChem* **13**, 2824–2875 (2012).
17. Tammeveski, K. *et al.* The reduction of oxygen on Pt-TiO₂ coated Ti electrodes in alkaline solution. *J. Electrochem. Soc.* **146**, 669–676 (1999).
18. Mentus, S. V. Oxygen reduction on anodically formed titanium dioxide. *Electrochim. Acta* **50**, 27–32 (2004).
19. Wang, B. Recent development of non-platinum catalysts for oxygen reduction reaction. *J. Power Sources* **152**, 1–15 (2005).
20. Pan, X. Y., Yang, M. Q., Fu, X. Z., Zhang, N. & Xu, Y. J. Defective TiO₂ with oxygen vacancies: synthesis, properties and photocatalytic applications. *Nanoscale* **5**, 3601–3614 (2013).
21. Wang, G. M., Ling, Y. C. & Li, Y. Oxygen-deficient metal oxide nanostructures for photoelectrochemical water oxidation and other applications. *Nanoscale* **4**, 6682–6691 (2012).
22. Nowotny, J. Titanium dioxide-based semiconductors for solar-driven environmentally friendly applications: impact of point defects on performance. *Energy Environ. Sci.* **1**, 565–572 (2008).
23. Xing, M. Y. *et al.* Self-doped Ti³⁺-enhanced TiO₂ nanoparticles with a high-performance photocatalysis. *J. Catal.* **297**, 236–243 (2013).
24. Liu, G. *et al.* Enhanced photoactivity of oxygen-deficient anatase TiO₂ sheets with dominant {001} facets. *J. Phys. Chem. C* **113**, 21784–21788 (2009).
25. Song, M. K. *et al.* Anomalous pseudocapacitive behavior of a nanostructured, mixed-valent manganese oxide film for electrical energy storage. *Nano Lett.* **12**, 3483–3490 (2012).
26. Fabio, H. B., Lima, M. L. C. & Ticianelli, E. A. Investigations of the catalytic properties of manganese oxides for the oxygen reduction reaction in alkaline media. *J. Electroanal. Chem.* **590**, 152–160 (2006).
27. Han, X. P., Zhang, T. R., Du, J., Cheng, F. Y. & Chen, J. Porous calcium-manganese oxide microspheres for electrocatalytic oxygen reduction with high activity. *Chem. Sci.* **4**, 368–376 (2013).
28. Gorlin, Y. & Jaramillo, T. F. A bifunctional nonprecious metal catalyst for oxygen reduction and water oxidation. *J. Am. Chem. Soc.* **132**, 13612–13614 (2010).
29. Stoerzinger, K. A. *et al.* Oxygen electrocatalysis on (001)-oriented manganese perovskite films: Mn valency and charge transfer at the Nanoscale. *Energy Environ. Sci.* **6**, 1582–1588 (2013).
30. El-Deab, M. S. & Ohsaka, T. Manganese oxide nanoparticles electrodeposited on platinum are superior to platinum for oxygen reduction. *Angew. Chem. Int. Ed.* **45**, 5963–5966 (2006).
31. Xiao, W., Wang, D. L. & Lou, X. W. Shape-controlled synthesis of MnO₂ nanostructures with enhanced electrocatalytic activity for oxygen reduction. *J. Phys. Chem. C* **114**, 1694–1700 (2010).
32. Duan, J. J. *et al.* Mesoporous hybrid material composed of Mn₃O₄ nanoparticles on nitrogen-doped graphene for highly efficient oxygen reduction reaction. *Chem. Commun.* **49**, 7705–7707 (2013).
33. Tian, Z. R. *et al.* Manganese oxide mesoporous structures: Mixed-valent semiconducting catalysts. *Science* **276**, 926–930 (1997).
34. Liu, S. W., Yu, J. G. & Jaroniec, M. Anatase TiO₂ with dominant high-energy {001} facets: synthesis, properties, and applications. *Chem. Mater.* **23**, 4085–4093 (2011).
35. Zheng, Z. K. *et al.* Metallic zinc-assisted synthesis of Ti³⁺ self-doped TiO₂ with tunable phase composition and visible-light photocatalytic activity. *Chem. Commun.* **49**, 868–870 (2013).
36. Goux, A., Pauporté, T. & Lincot, D. Oxygen reduction reaction on electrodeposited zinc oxide electrodes in KCl solution at 70°. *Electrochim. Acta* **51**, 3168–3172 (2006).
37. Jafri, R. I., Sujatha, N., Rajalakshmi, N. & Ramaprabhu, S. Au-MnO₂/MWNT and Au-ZnO/MWNT as oxygen reduction reaction electrocatalyst for polymer electrolyte membrane fuel cell. *Inter. J. Hydro. Ener.* **34**, 6371–6376 (2009).
38. Pan, C. & Zhu, Y. New type of BiPO₄ oxy-acid salt photocatalyst with high photocatalytic activity on degradation of dye. *Environ. Sci. Technol.* **44**, 5570–5574 (2010).
39. Zhang, A. Y., Long, L. L., Liu, C., Li, W. W. & Yu, H. Q. Electrochemical degradation of refractory pollutants using TiO₂ single crystals exposed by high-energy {001} facets. *Wat. Res.* **66**, 273–282 (2014).
40. Sun, Y. F. *et al.* Pits confined in ultrathin cerium (IV) oxide for studying catalytic centers in carbon monoxide oxidation. *Nat. Commun.* **4**, 2899 (2013).
41. Perdew, J. P., Burke, K. & Ernzerhof, M. Generalized gradient approximation made simple. *Phys. Rev. Lett.* **77**, 3865–3868 (1996).
42. Aschauer, U. *et al.* Influence of subsurface defects on the surface reactivity of TiO₂: water on anatase (101). *J. Phys. Chem. C* **114**, 1278–1284 (2010).
43. Halgren, T. A. & Lipscomb, W. N. Synchronous-transit method for determining reaction pathways and locating molecular transition-states. *Chem. Phys. Lett.* **49**, 225–232 (1977).

Acknowledgements

We thank the National Basic Research Program of China (2011CB933702), the NSFC (51208488) and the Program for Changjiang Scholars and Innovative Research Team in University and the Collaborative Innovation Center of Suzhou Nano Science and Technology of the Ministry of Education of China for supporting this work.

Author contributions

A.-Y.Z. and H.-Q.Y. conceived the idea. A.-Y.Z., D.-N.P. and X.Z. planned and performed the experiments, collected and analysed the data. L.G. and J.-J.C. performed the DFT calculations. A.-Y.Z., H.-Q.Y. and Y.M. co-wrote the manuscript. All authors discussed the results and commented on the manuscript.

Additional information

Supplementary Information accompanies this paper at <http://www.nature.com/naturecommunications>

Competing financial interests: The authors declare no competing financial interests.

Reprints and permission information is available online at <http://npg.nature.com/reprintsandpermissions/>

How to cite this article: Pei, D.-N. *et al.* Defective titanium dioxide single crystals exposed by high-energy {001} facets for efficient oxygen reduction. *Nat. Commun.* **6**:8696 doi: 10.1038/ncomms9696 (2015).



This work is licensed under a Creative Commons Attribution 4.0 International License. The images or other third party material in this article are included in the article's Creative Commons license, unless indicated otherwise in the credit line; if the material is not included under the Creative Commons license, users will need to obtain permission from the license holder to reproduce the material. To view a copy of this license, visit <http://creativecommons.org/licenses/by/4.0/>